

UCLA

UCLA Previously Published Works

Title

Thermohydraulic characteristics of a multi-string direct-contact heat exchanger

Permalink

<https://escholarship.org/uc/item/8985m212>

Authors

Zeng, Zezhi
Sadeghpour, Abolfazl
Ju, Y Sungtaek

Publication Date

2018-11-01

DOI

10.1016/j.ijheatmasstransfer.2018.05.060

Peer reviewed

THERMOHYDRAULIC CHARACTERISTICS OF A MULTI-STRING DIRECT-CONTACT HEAT EXCHANGER

ZeZhi Zeng, Abolfazl Sadeghpour, and Y. Sungtaek Ju*

Department of Mechanical and Aerospace Engineering
University of California, Los Angeles, CA 90095, USA

ABSTRACT

Direct-contact heat exchangers that involve energy exchange between gas and liquid streams have a variety of applications, including waste heat recovery, thermoelectric power plant cooling, and thermal desalination. Direct-contact heat exchangers are appealing as they may help mitigate potential corrosion, fouling, and scaling of solid surfaces and enhance heat transfer effectiveness. In this study, we experimentally investigate the thermohydraulic characteristics of an economic light-weight direct-contact heat exchanger that incorporates an array of strings of diameter of the order of 0.1~1 mm to sustain flows of thin liquid films. We constructed a 1.6 m-tall prototype heat exchanger with an array of as many as 112 vertically aligned strings. Thin films of a non-evaporating liquid are flown down the strings by gravity and exchange thermal energy with a counterflowing gas stream. We obtained axial liquid temperature profiles and frictional loss in the gas stream for different combinations of liquid and gas flow rates and two different string pitches. Numerical simulation is also performed to help interpret and indirectly validate our experimental results. The overall, gas-side, and liquid-side heat transfer coefficients extracted from the experimentally measured temperature profiles are examined to evaluate the impact of instability in liquid film flows and inter-bead spacing. The applicability of the Reynolds analogy is also assessed using the measured gas-stream pressure drops and air-side heat transfer coefficients. The present study helps improve our understanding of heat transfer and gas-stream pressure drop in string-based direct-contact heat exchangers and provides an experimental database to help systematically optimize their design.

KEY WORDS: Direct-contact heat exchanger, interfacial heat transfer, dry cooling, thin film flows

1. INTRODUCTION

The low thermal conductivity and low volumetric heat capacity of gases makes it difficult to design effective heat exchangers involving gas streams. Direct-contact heat exchangers are good candidates in certain applications, such as indirect dry cooling of thermoelectric power plants; waste heat capture; and heating or cooling of gaseous feed stocks or products in chemical processing. Packed beds are widely used in various direct-contact heat transfer applications [1–3] because their tortuous flow paths help achieve high heat transfer effectiveness. However, relatively high pressure drops experienced by the gas streams and low limits on gas loadings due to liquid flooding remain major challenges [4, 5]. Spray columns achieve heat transfer by dispensing small droplets into gas streams [6] but they can experience practical challenges: excess liquid pumping power required for spray generation; potential environmental issues associated with small droplets carried away with gas streams; and degraded heat transfer performance due to short residence time of large droplets [7]. New concepts and designs for direct-contact heat exchangers that can deliver high heat exchanger effectiveness while circumventing these challenges are desirable.

One promising alternative design of direct-contact heat exchangers is a multi-string column schematically illustrated in Fig.1. Each unit consists of a dense array of vertically aligned polymer strings of radii of the order of 0.1 mm. A heated non-volatile coolant is fed into each unit through top liquid distributors. As it travels down along the strings, the coolant is cooled by the counterflowing air stream. The straight and contiguous flow paths in-between the strings are expected to reduce pressure drops experienced by the gas streams than packed beds. At the same time, large gas/liquid interface-to-volume ratios and long residence times enable effective interfacial heat transfer process. The string arrays also limit radial liquid transport, facilitating more uniform liquid distributions. The use of polymer strings also reduces the cost and weight of the heat exchanger.

*Corresponding Author: sungtaek.ju@ucla.edu

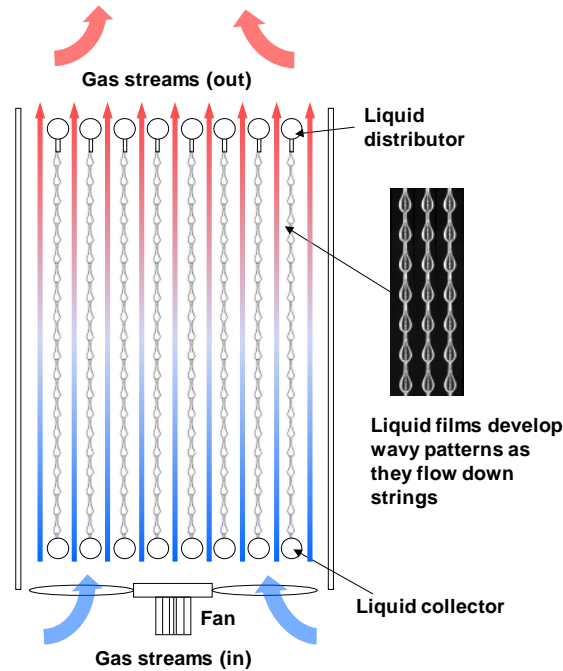


Fig. 1 Schematic of a multi-string heat exchanger unit.

To enable systematic design of the multi-string heat exchanger, we need a rigorous understanding of the fluid dynamics and heat transfer characteristics of liquid films flowing down vertical strings. Most early studies of heat transfer involving liquid films focus on planar surfaces or large diameter tubes [8–19]. Liquid films flowing on highly curved surfaces show wavy profiles due to intrinsic flow instability arising from interplay among surface tension, viscous, inertia, and gravitational force [7, 20, 21]. Two main flow regimes have been observed. In the Rayleigh-Plateau (RP) regime [22], liquid films develop liquid beads that travel along the string at the same speed with uniform inter-bead spacing. In the Kapitza instability regime [23], liquid films develop beads that travel at different velocities and two successive liquid beads may coalesce (and then re-separate) [24–26].

Several previous studies investigated liquid films flowing down strings in the Rayleigh Plateau regime for mass transfer applications with counterflowing air velocities below 1 m/s. One such study [27] experimentally investigated the CO₂ absorption by water films. It reported that multi-string mass exchangers achieved higher CO₂ absorption effectiveness than spray columns and packed beds under nominally the same operating conditions. A later study [5] reported the development and validation of an analytical model for the CO₂ absorption performance [27]. Another study [28] developed a numerical model for CO₂ absorption by water/monoethanolamine liquid films along a single string and performed a parametric study on absorption efficiency. More recent studies reported numerical fluid dynamics simulation of liquid films in the Kapitza instability regime under high counterflowing gas loads [29]. These studies also found the CO₂ absorption effectiveness to be higher for liquid films flowing on strings than liquid films on planar surfaces [20].

Migita et al. [30, 31] constructed a prototype multi-string mass exchanger containing an array of 109 strings to study CO₂ absorption and gas-stream pressure drop. They demonstrated that multi-string mass exchanger has higher absorption effectiveness and lower pressure drop than conventional packed beds. A more recent study [32] investigated hydrazine absorption by a multistring column, and confirmed the advantage of low air side pressure drop.

Relatively few previous studies focused on heat transfer in multi-string exchangers. Hattori et al. [33] presented an approximate analytical model for temperature distribution along a liquid film flowing down a string in the presence of cross-flows of a cooling gas. A modified version of the model in the counterflow configuration was validated in our previous study using a single-string [34]. A later study [7] constructed an experimental setup consisting of a single string and determined the liquid-to-gas overall heat transfer coefficient. The study reported enhanced heat transfer in wavy films in the Rayleigh-Plateau regime, which was ascribed to enhanced internal mixing. However, the study was limited in that it reported the experiments

at one fixed gas velocity and that it did not separate the gas-side and air-side thermal resistance. It also did not explore how convective instability, also referred to as the Kapitza instability, in liquid films flows affects heat transfer.

In the present article, we report our experimental study of a direct-contact multi-string heat exchanger. Although multi-string exchangers can generally be used in applications involving gas-liquid phase changes, such as evaporators and condensers, we will limit ourselves to non-evaporating liquids and non-condensing gases (air) in the present manuscript. We measure axial liquid temperature profiles and gas-stream pressure drop to examine the impact on the thermohydraulic performance of the liquid and air flow rates, instability modes, and string pitch. The applicability of the Reynolds analogy is also examined.

2. EXPERIMENTAL SETUP AND NUMERICAL SIMULATION

2.1 Experimental

A schematic of the experimental setup used in the present study is shown in Fig. 2. The setup consists of a vertical acrylic cylinder of diameter 10 cm; a top liquid reservoir; a bottom chamber with flow conditioners to ensure a uniform inlet air stream; and a square array of either 112 polymer strings (7 mm pitch) or 56 strings (10 mm pitch). The polymer strings ($R_w = 0.1$ mm) are fixed to a metal rod to keep them under tension. The liquid is pumped to the top reservoir, where a cartridge heater with a maximum rating of 2000 W is used to heat the liquid before it exits from the liquid nozzles. After exiting the nozzles, the liquid flows along the strings and is then collected at the bottom. The collected liquid is later recirculated to the top reservoir through a gear pump. Compressed air (inlet pressure ~ 1.3 bar, temperature ~ 20.8 °C) is fed in to the bottom chamber through four plastic tubes with an inner diameter of 3.8 cm. A variable-area flow meter with a range of 6 – 60 SCFM is used to measure the volumetric air flow rate. The superficial air velocity is calculated by dividing the measured volumetric air flow rate by the cross-sectional area of the acrylic cylinder.

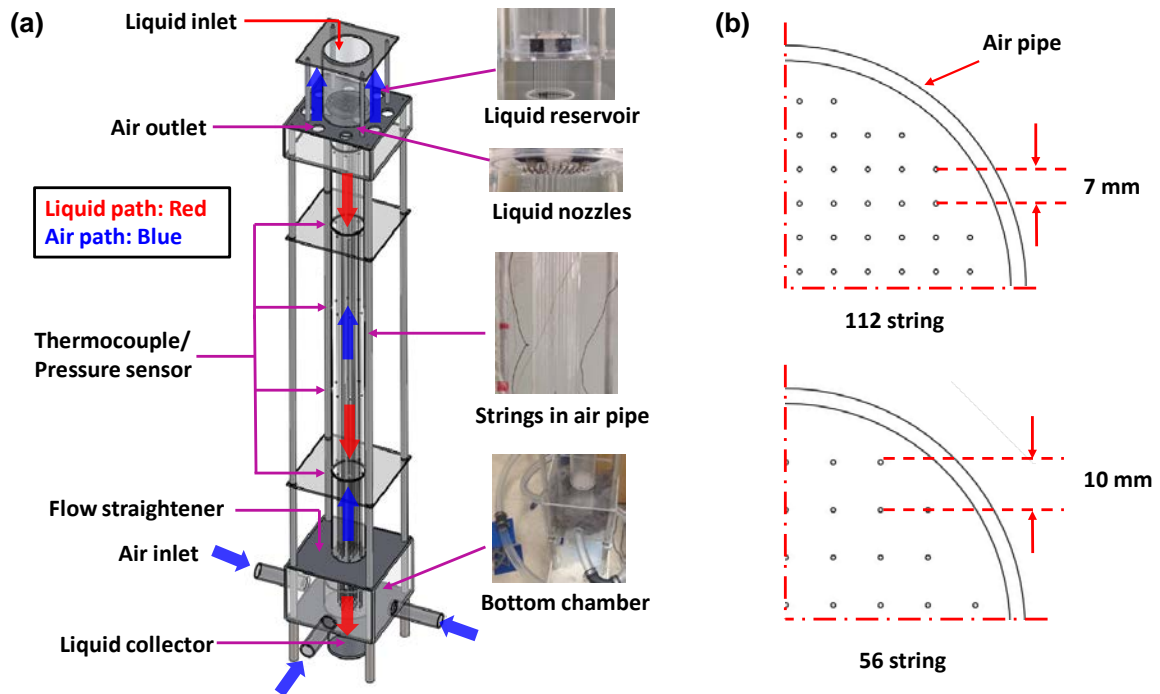


Fig. 2 (a) Schematic of the experimental setup we used for studying the heat transfer effectiveness and air-side pressure drop of a multi-string heat exchanger. (b) Top views of two arrays with different string pitches.

The liquid nozzles have a diameter of 1 mm and are made of stainless steel. The silicone oil is a well-wetting liquid and tends to rise along the nozzle outer surface, especially during a flow start-up phase where

the liquid flow rate is negligible (Fig. 3a). For our nozzles and working fluid, nozzle lengths greater than 2.5 mm are necessary to prevent the liquid from merging with the top plate and forming an undesired liquid puddle that can impede the liquid flow (Fig. 3b). The minimum necessary nozzle lengths are generally smaller for liquids with higher viscosities.

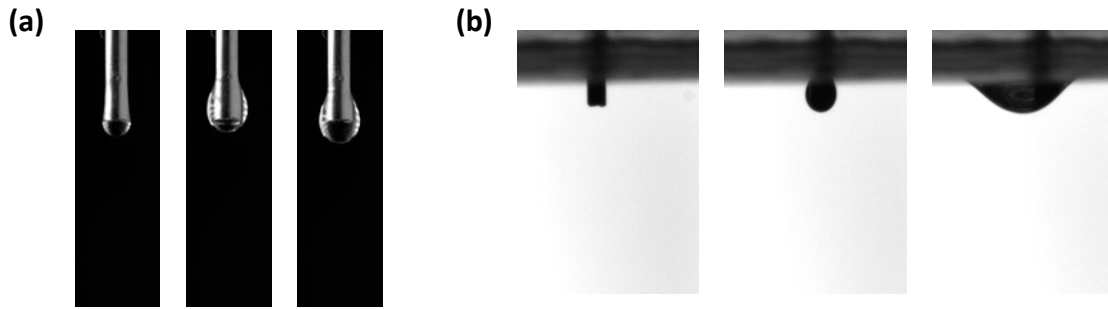


Fig. 3 (a) Capillary rise of silicone oil along the nozzle outer wall. (b) A liquid puddle formed around the nozzle can impede the liquid flow.

Four groups of 3 micro-thermocouples with tip diameter of 250 μm are placed at three radial locations (i.e. next to 3 different strings) and several axial locations (0.4 m, 0.7 m, 1.0 m, and 1.3 m from the liquid nozzle) as indicated in Fig. 2) to measure the liquid temperatures. We position the micro-thermocouples nominally 0.1 mm away from the strings. The micro-thermocouples are an order of magnitude smaller than liquid beads and they become fully immersed in the liquid as liquid beads flow past them. The thermal response time of the micro-thermocouples ($r^2\rho c_p/3k$ for a sphere immersed in a much larger medium) is estimated to be 0.03 second, which is shorter than the liquid bead transit time over each micro-thermocouple (~ 0.1 second). Although the micro-thermocouple wires slightly drag a portion of a liquid bead off the string, we observe that the liquid bead returns to the string once it passes the micro-thermocouple when the inter-bead spacing is greater than approximately three times the liquid bead length (i.e. $L > 3L_b$, see Fig. 4). At a smaller inter-bead spacing, the liquid film flow can be disturbed substantially, and two successive beads may merge. In all the experiment reported in the manuscript, the inter-bead spacing is at least four times larger than the bead length. Nevertheless, we positioned the twelve micro-thermocouples at different strings to avoid any potential complication from upstream micro-thermocouples.

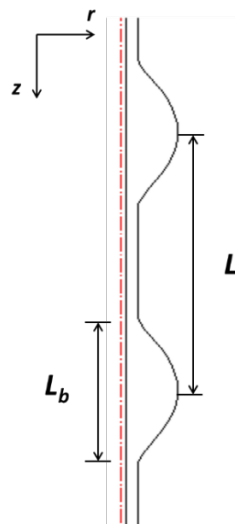


Fig. 4 The geometric parameters of the travelling beads

A previous study by Nozaki et al. [7] and our numerical simulation study [34] indicated that spatial temperature variations within a liquid bead is less than 2% of the bead mean temperature. At measurement locations, secondary flows generated by interactions with the micro-thermocouples are expected to further

enhance mixing and temperature uniformity. Measured fluctuations in micro-thermocouple readings are less than 0.1 °C. We also note that, under the experimental conditions used in the present study, liquid beads account for nearly 95% of the total liquid mass flow. The rest is carried by a thin contiguous liquid substrate flowing down the string. This liquid substrate is periodically entrained by and mixes with liquid beads. Given these, we consider the measured liquid bead temperature as a good approximation of the local bulk mean temperature of the liquid film at the corresponding axial location.

Three thermocouples are also placed inside the top liquid reservoir to monitor liquid inlet temperature. The heater power is adjusted for each run to maintain the liquid temperature inside the top reservoir at 41°C. Outputs from the thermocouples are monitored using a 24-bit high data acquisition system.

Two pressure transducers are placed along axial locations 1 m apart to measure gas-stream pressure drops for each run. The liquid flow rate is measured using a weight scale with a resolution of 0.1 g placed under the liquid collector. The liquid used in our study is low surface tension Rhodorsil v50 silicone oil. Its key properties are: density $\rho = 963 \text{ kg/m}^3$, kinematic viscosity $\nu = 50 \text{ mm}^2/\text{s}$, surface tension $\gamma = 20.8 \text{ mN/m}$ at 20 °C, thermal conductivity $k = 0.15 \text{ W/(m}\cdot\text{K)}$, and specific heat $C_{pL} = 1507 \text{ J/(kg}\cdot\text{K)}$.

For each experimental run, the liquid and air flow rate were first adjusted to respective desire values. The measurements were taken after the readings from all the thermocouples and pressure transducers were stabilized to within 1% over a 15 minutes period. At each liquid and air flow rate combination, experiments were repeated at least three times to confirm reproducibility in temperature and pressure readings to within 5%. Uncertainty in thermocouple readings is estimated to be $\pm 0.1^\circ\text{C}$. Radial variations in the liquid temperature, which may be attributed to slight differences in the liquid flow rate among the strings, is estimated to be $\pm 0.5^\circ\text{C}$ for flows in the Rayleigh-Plateau regime and $\pm 1^\circ\text{C}$ in the Kapitza instability regime. Uncertainty in the measured pressure drops is estimated to be 0.05 Pa at the air velocity of 0.4 m/s and 0.5 Pa at the air velocity of 4 m/s. Uncertainty in the measured air velocities is estimated to be 0.1 m/s, and uncertainty in the measured liquid flow rates 0.1 g/s.

2.2 Numerical simulation

To help interpret and indirectly validate our experimental results, we constructed a 3D steady-state numerical model to simulate flow and heat transfer characteristics of the multi-string heat exchanger. For each liquid flow rate, we assumed flat liquid films with the same interfacial areas as wavy films observed in the actual experiment. To reduce computational times, we selected a quarter of the one string unit for our simulation, as illustrated in Fig.5 (a). Figure 5 (b) shows the simulation domain and the corresponding boundary conditions. The adiabatic and no slip condition are applied at the string surface. The zero shear stress and adiabatic condition are applied at all the symmetry surfaces. The coupled-wall condition is applied at the liquid film and air interface to ensure velocity, shear stress, and temperature continuity.

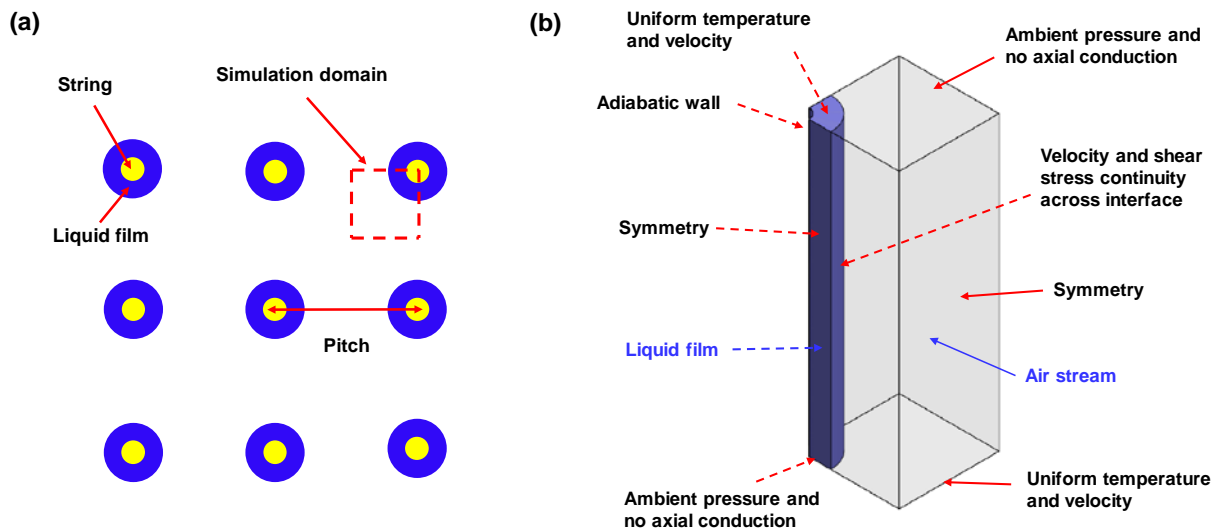


Fig. 5 Schematic of the simulation domain of the multi-string heat exchanger and the corresponding boundary conditions.

A commercial computational fluid dynamics package (ANSYS-Fluent) was used in our simulation. We solved the steady state Navier-Stokes equations and the energy conservation equations to obtain the temperature distributions in both the liquid film and the air stream. Air flows in our experiment are expected to transition to turbulent flow at a Reynolds number of 2300. We used a laminar flow module for the cases with laminar air stream and the transitional shear stress transport (SST) model [35, 36] for the cases with turbulent air flow. For improved accuracy, we use the $k-\omega$ model close to the solid surfaces and the $k-\epsilon$ model in the free stream [37].

A multi-zone mesh method was used in the current simulation, which consisted of mainly hexahedral meshes and some tetrahedral meshes. Approximately four million elements used in typical simulation runs. The element size varied gradually from $5\ \mu\text{m}$ in the liquid film to $250\ \mu\text{m}$ in air. At the liquid-gas interface, 25 boundary layers were applied with the first layer thickness smaller than $1\ \mu\text{m}$ to resolve the turbulent viscous sublayer. A mesh-independence study and numerical convergence study were performed to ensure that the predicted liquid film temperatures do not change by more than 2% with further mesh refinements and larger iteration numbers.

3. RESULTS AND DISCUSSION

3.1 Axial profiles of the dimensionless temperature

We first analyze the operation of the multi-string heat exchanger under different combinations of the total liquid and air flow rates for its interpretation as a counterflow heat exchanger. To quantify the heat transfer performance of a multistring heat exchanger, we use a dimensionless liquid temperature [38] defined as:

$$\theta(z) = \frac{T_L(z) - T_{G,in}}{T_{L,in} - T_{G,in}} \quad (1)$$

Here, $T_L(z)$ denotes the liquid temperature at a specific axial location z . $T_{L,in}$, and $T_{G,in}$ denote the inlet liquid temperature and the inlet gas temperature, respectively.

Figure 6 (a) shows the dimensionless temperature as a function of the axial location z for a given liquid flow rate but three different air velocities. Figure 6 (b) shows the dimensionless temperature as a function of the axial location z for a given air velocity but three different liquid flow rates. The dimensionless temperature at the liquid outlet is lower for higher air velocities and lower liquid flow rates, consistent with the general behavior of counterflow heat exchangers.

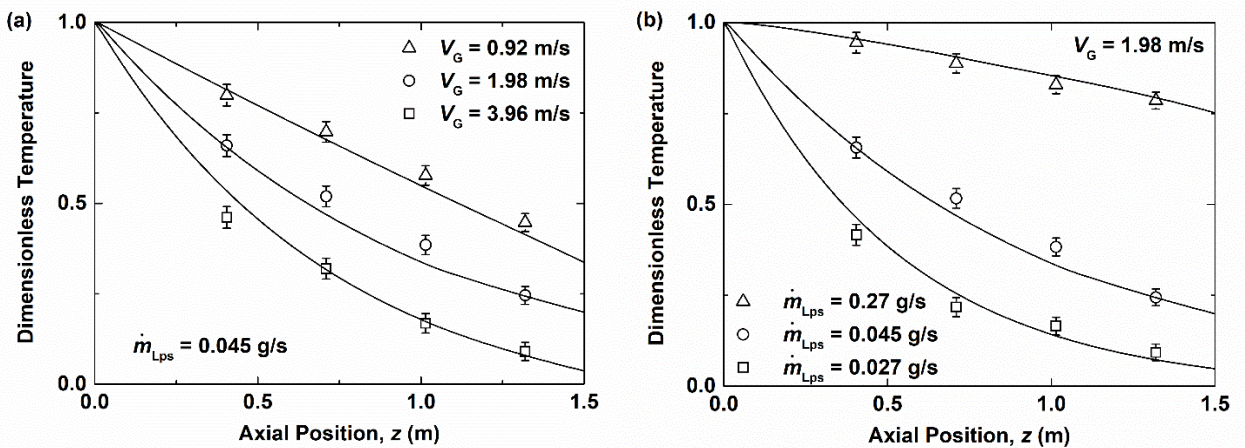


Fig. 6 (a) Dimensionless liquid temperature as a function of the axial location for a given liquid flow rate under three different air velocities. (b) Dimensionless liquid temperature as a function of the axial location for a given superficial air velocity of 1.98 m/s under three different liquid flow rates. Here \dot{m}_{Lps} denotes the liquid mass flow rate per string. The symbols represent experimental data and the solid lines the simulation results. All the experimental results shown here are from the square array of 112 strings (7 mm pitch).

Figure 7 shows the dimensionless temperature as a function of the axial location for three groups of data. Each group consists of a data set obtained from the 7 mm-pitch array (112 strings in total) and a data set obtained using a 10 mm-pitch array (56 strings in total). In all cases, the liquid flow rate per string are fixed at 0.045 g/s. When the air flow rates are adjusted to keep the heat capacity rate ratio C_r constant, the dimensionless temperatures from the two string arrays remain within 5% of each other. This suggests that the overall heat transfer coefficient does not depend sensitively on the string pitch and hence the hydraulic diameter for the present two cases. The lines represent the numerical simulation results, which agree well with our experimental data. The experimentally measured temperature profiles shown here are further analyzed to extract the heat transfer coefficients in Section 3.2.

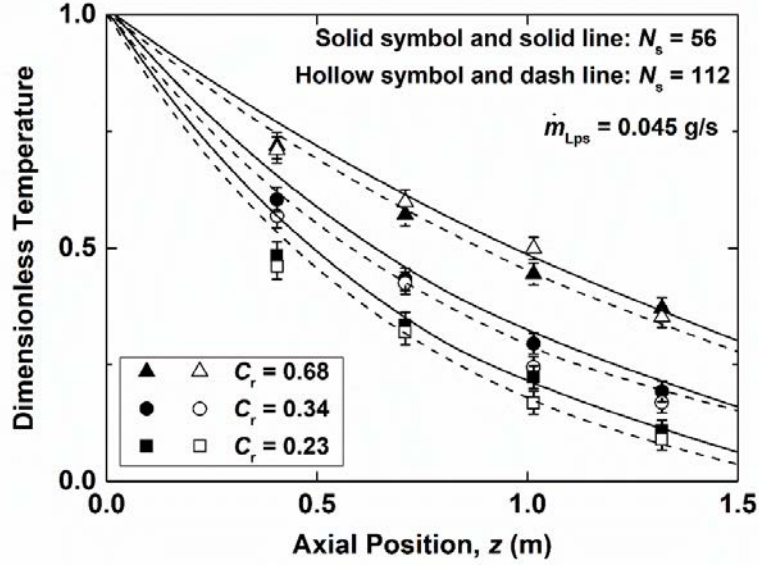


Fig. 7 Dimensionless liquid temperature as a function of the axial location. The symbols correspond to the experimental data. The solid lines represent the simulation results for the array of strings with 10 mm pitch and the dash lines the simulation results for the array of strings with 7 mm pitch. \dot{m}_{Lps} denotes the liquid flow rate per string, which is fixed, and N_s the total number of strings. For all the data shown in Fig. 7, the smaller of the heat capacity rates, C_{min} , is that of the liquid.

We next consider cases where we vary the liquid flow rate per string while adjusting the air velocity to keep the heat capacity rate ratio constant. Figure 8 shows the dimensionless temperature as a function of the axial location for three different liquid flow rates per string under a fixed heat capacity rate ratio. The liquid film with a liquid flow rate of 0.045 g/s is in the Rayleigh-Plateau regime whereas the liquid films with the two higher liquid flow rates exhibit the Kapitza instability regime. All three sets of data shown in Fig. 8 are obtained using the square string array of 7 mm pitch (112 strings in total).

The dimensionless temperatures deviate from each other as we move down the strings, with the highest flow rate case showing almost 20% higher dimensionless temperature than the lowest flow rate case near the liquid outlet. This is attributed to transition from the Rayleigh-Plateau regime to the Kapitza instability regime. Although the instability transition enhances heat transfer coefficient (as discussed in Sec 3.2), the reduced surface area to volume ratios and shorter liquid residence times on the string lead to a higher dimensionless temperature.

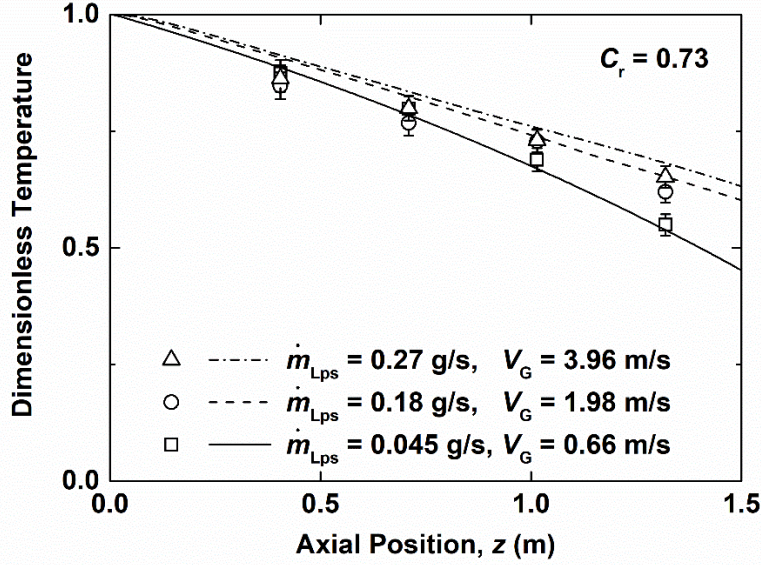


Fig. 8 Dimensionless liquid temperature as a function of the axial location for three different liquid flow rates per string. The symbols represent the experimental data and the lines represent the numerical simulation result. The three cases share the same heat capacity rate ratio. The smaller of the two heat capacity rates, C_{\min} , is that of air for the cases shown.

3.2 Heat transfer coefficients

To further elucidate the impact of the liquid film thickness and morphology, hence the instability regime, on heat transfer, we analyze the axial temperature profiles to extract the overall heat transfer coefficients. Under the assumptions of the constant overall heat transfer coefficient and no axial conduction, the energy conservation equations [39] can be written as

$$\dot{m}_L C_{p,L} dT_L = U dA \Delta T_{\text{local}} \quad (2)$$

$$\dot{m}_L C_{p,L} dT_L = \dot{m}_A C_{p,A} dT_A \quad (3)$$

Here \dot{m}_L , T_L , $C_{p,L}$, denote the flow rate, temperature, and specific heat of the liquid, respectively. Likewise, the parameters \dot{m}_A , T_A , and $C_{p,A}$ denote the corresponding quantities for air. U represents the overall heat transfer coefficient and ΔT_{local} represents the local temperature difference between the liquid film and the air stream. We iteratively solved these two equations numerically using U as an adjustable parameter until the liquid film temperature matched the experimental data. The quality of the fits is comparable to that of the numerical simulation results shown in Figs. 7 and 8.

The gas side heat transfer coefficient in general depends non-linearly on the air velocity. Figure 9 shows the reciprocal of overall heat transfer coefficients as a function of $1/V_G^m$ where V_G is the superficial air velocity. We use a previously reported value of 0.8 for the exponent m in turbulent flows [40]. Following a previous study [17], we consider the y-intercept, corresponding to the infinite air velocity, of the linear fit to each data set as a measure of the liquid-side heat transfer coefficient (or its reciprocal, to be precise). For the liquid films flowing in the Rayleigh-Plateau regime shown in Fig. 9(a), the estimated liquid-side heat transfer coefficients are 37 – 55 W/(m² K). The string array pitch (7 or 10 mm) has a negligible effect on the liquid side heat transfer coefficient.

The estimated liquid-side heat transfer coefficients values are comparable to the conduction resistance of approximately 30 W/(m² K) across liquid spheres of the same equivalent radii as travelling liquid beads. The actual liquid-side heat transfer coefficient would be higher than this value because internal circulation within

each bead enhances heat transfer [33]. Note that, for a fixed nozzle diameter, liquid films flowing in the Rayleigh-Plateau regime at different flow rates produce liquid beads of approximately the same radii but different inter-bead spacings [21, 34].

We note that the cases with a liquid flow rate per string of 0.027 g/s show larger overall heat transfer coefficients than the case with a higher liquid flow rate per string of 0.045 g/s. This results from the smaller spacing between two successive liquid beads at the higher flow rate. As discussed in [34], at a smaller inter-bead spacing, downstream liquid beads are strongly affected by wakes (i.e., recirculation zones in the gas stream) formed behind upstream liquid beads [41, 42]. The convective heat transfer in the gas phase is therefore degraded.

At air velocities smaller than 1.2 m/s, the overall heat transfer coefficient of the heat exchanger with 10 mm string pitch (56 strings) is larger than that with 7 mm pitch (112 strings). This rather surprising result arises because transition to turbulence occurs at lower air velocities for the heat exchanger with the larger string pitch, which has an approximately 1.5 times larger hydraulic diameter than the heat exchanger with the smaller string pitch. At higher air velocities, when the air flows are turbulent in both heat exchangers, the overall heat transfer coefficients are comparable and nearly within their estimated uncertainties.

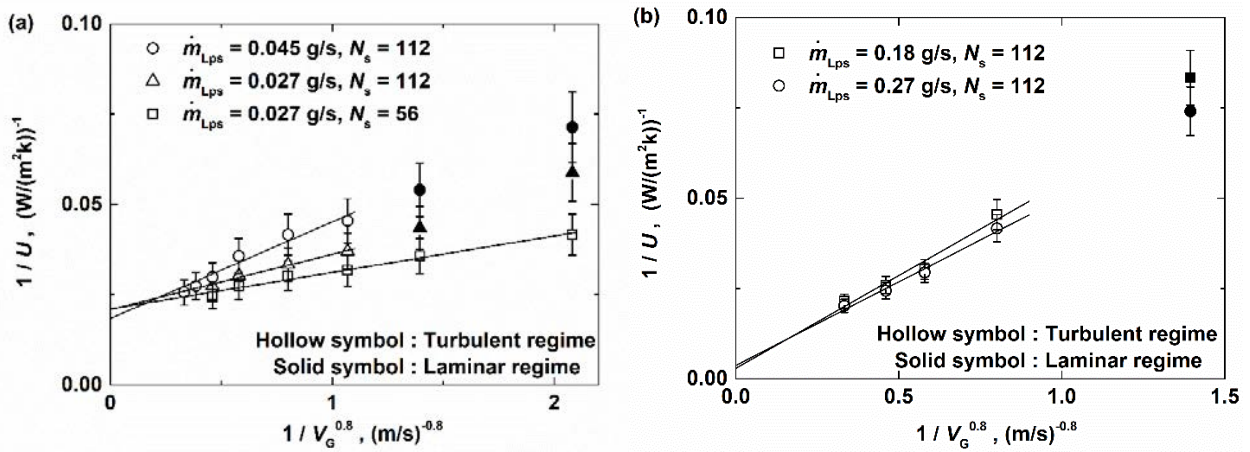


Fig. 9 The reciprocal of the overall heat transfer coefficient as a function of the reciprocal of the superficial air velocity. Part (a) shows the cases of liquid films flowing in the Rayleigh-Plateau regime whereas Part (b) shows the cases of liquid films flowing in the Kapitza instability regime.

Figure 9(b) shows the overall heat transfer coefficient of the liquid films flowing in the Kapitza instability regime as a function of the reciprocal of the air velocity. Following a similar approach as Fig. 9(a), we estimate the liquid-side heat transfer coefficients from the y-intercepts. The estimated liquid-side heat transfer coefficients range 100 - 400 W/(m²K), up to an order of magnitude higher than those for the liquid films flowing in the Rayleigh Plateau regime. This enhanced heat transfer in the liquid can be attributed to coalescence of liquid beads traveling at different speeds in the Kapitza instability regime, as shown in Fig. 10.

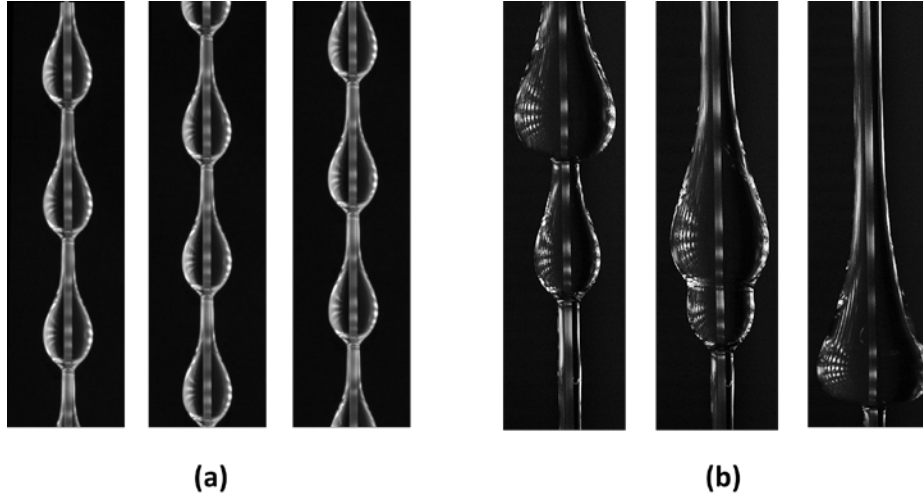


Fig. 10 Comparison between liquid films flowing (a) in the Rayleigh-Plateau regime and (b) in the Kapitza instability regime. The liquid bead coalescence only happens in the latter regime.

3.3 Air-side pressure drop

Gas-stream pressure drop is another important characteristic of heat or mass exchangers. Figure 11 shows our experimental data we obtain using the two string arrays of different pitches as a function of the air velocity. We compare the measured pressure drops with predictions from existing empirical correlations for longitudinal flows along rod bundles [45–48].

For laminar flows along an infinite extension of rod bundles, we adapt the reported correlation [45] for our multi-scale heat exchangers as

$$Re = \frac{\rho u D_h}{\mu} \quad (4)$$

$$\sigma = 1 - \frac{\pi}{4 \left(\frac{s}{D_N}\right)^2} \quad (5)$$

$$f_L Re \left(\frac{D_N}{D_h}\right) = \frac{8\sigma^2}{2(1-\sigma) - \ln(1-\sigma) - 0.5(1-\sigma)^2 - 1.5} \quad (6)$$

$$\frac{\Delta P}{\Delta z} = \frac{2f_L \rho u^2}{D_h} \quad (7)$$

Here, Re represents the gas stream Reynolds number based on the hydraulic diameter. D_h and D_N represent the hydraulic diameter and the average liquid film diameter calculated from Nusselt solution, respectively [25]. The parameter s denotes the center-to-center distance between two adjacent strings, u the air velocity, and f_L the friction factor in the laminar flow regime.

The gas flows in our multi-string exchangers are considered to undergo transition to turbulence at a Reynolds number of 2300. The air streams for the 10 mm-pitch string array are expected to be in the turbulent regime for all the experimental conditions reported here. For the 7 mm-pitch string array, the cases where the air flows are in the laminar flow regime are indicated in Fig. 11 using the solid symbols.

For turbulent flows along an infinite extension of rod bundles, the correlation reported in [46–48] for our multi-string heat exchangers is

$$x = \sqrt{\frac{\pi}{4}} \frac{s}{D_N} \quad (8)$$

$$\sqrt{\frac{8}{f_T}} = 2.5 \ln \left(Re \sqrt{\frac{f_T}{8}} \right) + 5.5 - \frac{3.966 + 1.25x}{1+x} - 2.5 \ln(2 + 2x) \quad (9)$$

$$\frac{\Delta P}{\Delta z} = \frac{f_T \rho u^2}{2D_h} \quad (10)$$

Here x denotes the geometric factor and f_T the friction factor in the turbulent regime

Figure 11 shows that the gas-stream pressure drop increases approximately linearly with increasing air velocities in the laminar flow regime. When the air flow reaches the turbulent regime, the pressure drop increases approximately quadratically with increasing air velocities.

Figure 11 also shows that, at a fixed array pitch and an air velocity, a larger liquid flow rate per string leads to a higher gas-phase pressure drop. Larger liquid flow rates per string lead to thicker liquid films, which not only reduce the cross-sectional area for gas flows but also increases the liquid-air interface areas. At a given liquid flow rate per string, the array with the larger string pitch has a lower pressure drop.

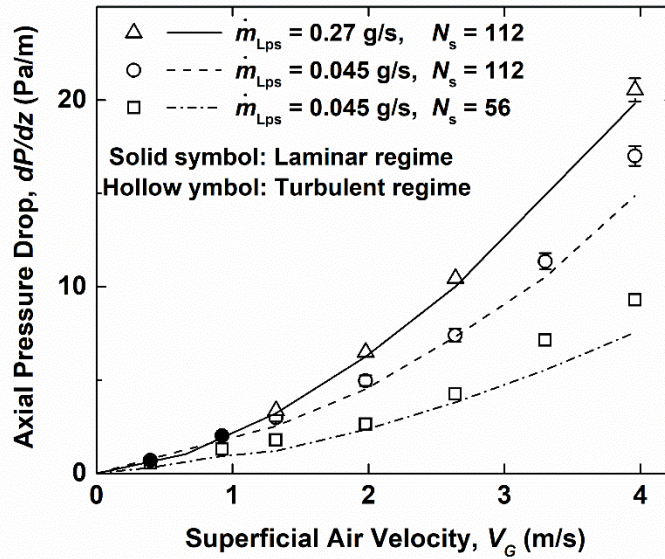


Fig. 11 Experimentally measured air-stream pressure drop (symbols) and the prediction from the empirical correlations (lines).

As shown in Fig. 11 the experimental data and the predictions from the empirical models for rod bundles match each other within 10%. The reasonably good agreement between the experimental data and the prediction does suggest relatively low form drag at superficial air velocities (< 3 m/s) used in the present study. In our experiments the inter-bead spacing is at least four times larger than the bead length as discussed in Sec 2.1. Under this condition, our numerical simulation [34] indicates that the skin friction dominates over the form drag as the flow separation angle (measured from the forward stagnation point) is large and the recirculation zone is narrow (Fig. 12a). For an example case (liquid flow rate per string = 0.044 g/s, superficial gas velocity = 1.32 m/s), the form drag is predicted to account for approximately 20% of the pressure drop. This is somewhat counteracted by the fact that the assumed smooth cylindrical rods have larger interfacial areas than the actual liquid films with discrete liquid beads, leading to approximately 10% “over”-prediction of the skin friction. These are consistent with the fact that the empirical model does underpredict the measured pressure drops by approximately 10%.

The situation is different at higher air velocities (larger than approximately 3 m/s) for liquid films flowing in the Rayleigh-Plateau regime. This may be attributed to finite bead deformation caused by aerodynamic drag as illustrated in Fig. 12 (b). This leads to much larger form drag. Indeed, the measured pressure drops are almost 20% larger than the model predictions. For liquid films flowing in the Kapitza instability regime, the liquid bead deformation is observed to be less pronounced, which may be due to their larger inertia and flatter

profiles as illustrated in Fig. 12 (c). The model prediction agrees better with the measured data in the Kapitza instability regime.

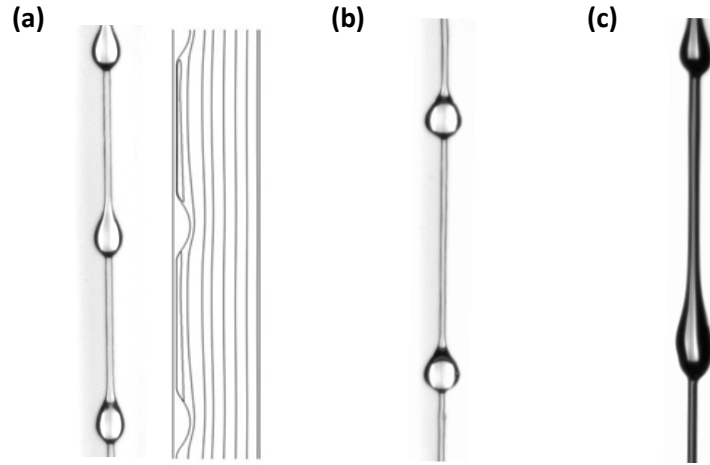


Fig. 12 (a) Predicted streamlines for a liquid film flowing in the Rayleigh-Plateau regime at a large inter-bead spacing and a low (< 3 m/s) gas velocity (b) Deformed liquid beads at a higher (> 3 m/s) gas velocity. (c) A typical liquid film profile with Kapitza instability

3.4 Air-side heat transfer coefficient and Reynolds analogy

Using the liquid side heat transfer coefficients we estimated in Sec. 3.2, we next calculate the corresponding air-side heat transfer coefficient from

$$\frac{1}{h_{\text{air}}} = \frac{1}{U} - \frac{1}{h_{\text{L}}} \quad (11)$$

Here h_{air} , U , and h_{L} are the air-side heat transfer coefficient, overall heat transfer coefficient, and liquid-side heat transfer coefficient, respectively. The calculated air-side heat transfer coefficients have very large uncertainty at high air velocities when the overall heat transfer coefficient is very close to the liquid side heat transfer coefficient. We therefore perform this calculation for air velocities below 1.98 m/s when the liquid flow rate per string is lower than 0.05 g/s.

As shown in Fig. 13, the air-side heat transfer coefficients thus calculated are consistent with the modified Reynold analogy, $C_f/2 = j_H$ [43, 44]. Here, j_H is the Colburn j factor and C_f is the Fanning friction factor [39]: The apparent applicability of the Reynolds analogy may be attributed to relatively small contribution from the form drag afforded by liquid beads under the experimental conditions used in the present study as discussed in Sec. 3.3.

$$j_H = StPr^{\frac{2}{3}} \quad (12)$$

$$St = \frac{h_{\text{air}}}{\rho_G c_{pG} V_G} \quad (13)$$

$$C_f = \frac{\Delta P A_c}{A(\frac{1}{2}\rho_G V_G^2)} \quad (14)$$

In the above, St is the Stanton number, Pr is the Prandtl number of air, A_c denotes the cross-sectional area of the gas stream, A denotes the total liquid-air interfacial area, and ΔP is the gas-stream pressure drop.

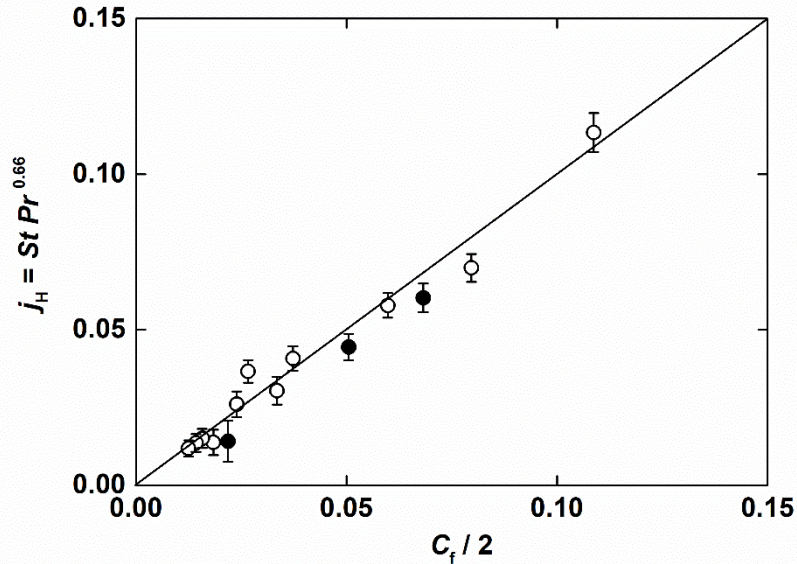


Fig. 13 Relationship between the Colburn j factor and the Fanning friction factor from our experiments. The solid line is a line of slope unity. The hollowed symbols are for air flows projected to be in the turbulent regime and the solid symbols in the laminar regime.

4. CONCLUSIONS

We experimentally investigated the influence of liquid flow rate, gas velocity and string pitch on the heat transfer performance and frictional loss of a multi-string heat exchanger. By analyzing the axial liquid temperature profiles, we extract the overall, liquid-side, and air side heat transfer coefficients under different combinations of air and liquid flow rates. The liquid films flowing in the Kapitza instability regime are found to have significantly smaller liquid-side thermal resistance than the liquid films flowing in the Rayleigh-Plateau regime. Merging of liquid beads traveling down the strings in the Kapitza instability regime is very effective in enhancing liquid-side thermal resistance. The overall heat transfer coefficient does not vary significantly between the two string pitches we examined (7 mm and 10 mm). For liquid films flowing in the Rayleigh-Plateau regime, the gas-side heat transfer coefficient is lower at higher liquid flow rates due to the increased interference of wake regions (of air) between successive liquid beads. The measured gas-stream pressure drop agrees reasonably well with the prediction from existing correlations for bundles of parallel solid tubes. The applicability of the Reynolds analogy for the gas streams has been observed under the present experimental conditions, which is consistent with a relatively small contribution of form drag afforded by the wavy liquid films. The present work helps improve our understanding of the heat transfer performance and frictional loss in a multi-string heat exchanger.

ACKNOWLEDGMENT

The present article is based on work supported in part by the National Science Foundation through grant CBET-1358034.

REFERENCES

- [1] K. Onda, H. Takeuchi, and Y. Okumoto, "Mass Transfer Coefficients Between Gas and Liquid Phases in Packed Columns," *J. Chem. Eng. Jpn.*, vol. 1, no. 1, pp. 56–62, 1968.
- [2] K. Onda, H. Takeuchi, and Y. Koyama, Effect of packing materials on the wetted surface area. *Kagaku Kogaku* 31, 126-134, 1967.
- [3] A. F. Mills, *Mass Transfer*, 1 edition. Upper Saddle River, N.J: Prentice Hall, 2001.

- [4] A. Mersmann and A. Deixler, "Packungskolonnen," *Chem. Ing. Tech.*, vol. 58, no. 1, pp. 19–31, Jan. 1986.
- [5] K. Uchiyama, H. Migita, R. Ohmura, and Y. H. Mori, "Gas absorption into 'string-of-beads' liquid flow with chemical reaction: application to carbon dioxide separation," *Int. J. Heat Mass Transf.*, vol. 46, no. 3, pp. 457–468, Jan. 2003.
- [6] R. Letan and E. Kehat, "The mechanics of a spray column," *AIChE J.*, vol. 13, no. 3, pp. 443–449, May 1967.
- [7] T. Nozaki, N. Kaji, and Y. H. Mori, "Heat Transfer to a Liquid Flowing Down Vertical Wires Hanging in a Hot Gas Stream: an Experimental Study of a New Means of Thermal Energy Recovery," *Proc. 11th Int. Heat Transfer Conf.*, vol. 6, pp. 63–68, 1998.
- [8] R. A. Seban and A. Faghri, "Evaporation and heating with turbulent falling liquid films," *J. Heat Transf.*, vol. 98, no. 2, pp. 315–318, 1976.
- [9] J. A. Shmerler and I. Mudawwar, "Local evaporative heat transfer coefficient in turbulent free-falling liquid films," *Int. J. Heat Mass Transf.*, vol. 31, no. 4, pp. 731–742, 1988.
- [10] J. A. Shmerler and I. Mudawwar, "Local heat transfer coefficient in wavy free-falling turbulent liquid films undergoing uniform sensible heating," *Int. J. Heat Mass Transf.*, vol. 31, no. 1, pp. 67–77, 1988.
- [11] S.-M. Yih and J.-L. Liu, "Prediction of heat transfer in turbulent falling liquid films with or without interfacial shear," *AIChE J.*, vol. 29, no. 6, pp. 903–909, 1983.
- [12] K. R. Chun and R. A. Seban, "Heat transfer to evaporating liquid films," *J. Heat Transf.*, vol. 93, no. 4, pp. 391–396, 1971.
- [13] T. Fujita and T. Ueda, "Heat transfer to falling liquid films and film breakdown—I: Subcooled liquid films," *Int. J. Heat Mass Transf.*, vol. 21, no. 2, pp. 97–108, 1978.
- [14] G. J. Gimbutis and A. D. S. Sinkunas, "Heat transfer of a turbulent water film at different initial flow conditions and high temperature gradients," *Proc. 6th Int. Heat*, 1978.
- [15] W. Wilke, "Warmeübertragung an rieselfilme," *VDI-Forschungsheft*, vol. 490, p. B28, 1962.
- [16] B. G. Ganchev, V. M. Koglov, and V. V. Lozovetskiy, "A study of heat transfer to a falling fluid film at a vertical surface," *Heat Transfer–Sov Res*, vol. 4, pp. 102–110, 1972.
- [17] W. I. Barnet and K. A. Kobe, "Heat and vapor transfer in a wetted-wall tower," *Ind. Eng. Chem.*, vol. 33, no. 4, pp. 436–442, 1941.
- [18] V. Patnaik, H. Perez-Blanco, and W. A. Ryan, "A simple model for the design of vertical tube absorbers," Oak Ridge National Lab., TN (United States), 1993.
- [19] R. Kafesjian, C. A. Plank, and E. R. Gerhard, "Liquid flow and gas phase mass transfer in wetted-wall towers," *AIChE J.*, vol. 7, no. 3, pp. 463–466, 1961.
- [20] J. Grünig, E. Lyagin, S. Horn, T. Skale, and M. Kraume, "Mass transfer characteristics of liquid films flowing down a vertical wire in a counter current gas flow," *Chem. Eng. Sci.*, vol. 69, no. 1, pp. 329–339, Feb. 2012.
- [21] A. Sadeghpour, Z. Zeng, and Y. S. Ju, "Effects of Nozzle Geometry on the Fluid Dynamics of Thin Liquid Films Flowing down Vertical Strings in the Rayleigh–Plateau Regime," *Langmuir*, vol. 33, no. 25, pp. 6292–6299, Jun. 2017.
- [22] J. W. Strutt and Lord Rayleigh, "On the instability of jets," *Proc Lond. Math Soc*, vol. 10, no. 4, 1878.
- [23] D. Ter Haar, *Collected papers of PL Kapitza*, vol. 2. Elsevier, 2013.
- [24] C. Duprat, C. Ruyer-Quil, S. Kalliadasis, and F. Giorgiutti-Dauphiné, "Absolute and Convective Instabilities of a Viscous Film Flowing Down a Vertical Fiber," *Phys. Rev. Lett.*, vol. 98, no. 24, p. 244502, Jun. 2007.
- [25] C. Duprat, C. Ruyer-Quil, and F. Giorgiutti-Dauphiné, "Spatial evolution of a film flowing down a fiber," *Phys. Fluids*, vol. 21, no. 4, p. 042109, Apr. 2009.
- [26] C. Duprat, C. Ruyer-Quil, and F. Giorgiutti-Dauphiné, "Experimental study of the instability of a film flowing down a vertical fiber," *Eur. Phys. J. Spec. Top.*, vol. 166, no. 1, pp. 63–66, Jan. 2009.
- [27] H. Chinju, K. Uchiyama, and Y. H. Mori, "'String-of-beads' flow of liquids on vertical wires for gas absorption," *AIChE J.*, vol. 46, no. 5, pp. 937–945, 2000.
- [28] S. M. Hosseini, R. Alizadeh, E. Fatehifar, and A. Alizadehdakhel, "Simulation of gas absorption into string-of-beads liquid flow with chemical reaction," *Heat Mass Transf.*, vol. 50, no. 10, pp. 1393–1403, Apr. 2014.
- [29] J. Grünig, T. Skale, and M. Kraume, "Liquid flow on a vertical wire in a countercurrent gas flow," *Chem. Eng. J.*, vol. 164, no. 1, pp. 121–131, 2010.
- [30] H. Migita, K. Soga, and Y. H. Mori, "Gas absorption in a wetted-wire column," *AIChE J.*, vol. 51, no. 8, pp. 2190–2198, Aug. 2005.
- [31] S. A. Galledari, R. Alizadeh, E. Fatehifar, and E. Soroush, "Simulation of carbon dioxide absorption by monoethanolamine solution in wetted-wire column," *Chem. Eng. Process. Process Intensif.*, vol. 102, pp. 59–69, 2016.
- [32] S. G. Pakdehi and S. Taheri, "Separation of Hydrazine from Air by Wetted Wire Column," *Chem. Eng. Technol.*, vol. 33, no. 10, pp. 1687–1694, Oct. 2010.
- [33] K. Hattori, M. Ishikawa, and Y. H. Mori, "Strings of liquid beads for gas-liquid contact operations," *AIChE J.*, vol. 40, no. 12, pp. 1983–1992, 1994.

- [34] Z. Zeng, A. Sadeghpour, G. Warrier, and Y. S. Ju, "Experimental study of heat transfer between thin liquid films flowing down a vertical string in the Rayleigh-Plateau instability regime and a counterflowing gas stream," *Int. J. Heat Mass Transf.*, vol. 108, Part A, pp. 830–840, May 2017.
- [35] F. R. Menter, "Two-equation eddy-viscosity turbulence models for engineering applications," *AIAA J.*, vol. 32, no. 8, pp. 1598–1605, 1994.
- [36] F. R. Menter, M. Kuntz, and R. Langtry, "Ten years of industrial experience with the SST turbulence model," *Turbul. Heat Mass Transf.*, vol. 4, no. 1, pp. 625–632, 2003.
- [37] A. Fluent, "ANSYS fluent theory guide 15.0," *Inc Canonsburg PA*, 2013.
- [38] W. M. Kays and A. L. London, "Compact heat exchangers," *McGraw-Hill, Inc*, Jan. 1984.
- [39] T. L. Bergman, F. P. Incropera, D. P. DeWitt, and A. S. Lavine, *Fundamentals of Heat and Mass Transfer 7th ed.* John Wiley & Sons, 2011.
- [40] A. Mills, *Heat and Mass Transfer*. CRC Press, 1995.
- [41] R. S. Ramachandran, C. Kleinstreuer, and T.-Y. Wang, "Forced Convection Heat Transfer of Interacting Spheres," *Numer. Heat Transf. Part Appl.*, vol. 15, no. 4, pp. 471–487, Jun. 1989.
- [42] B. Lloyd and R. Boehm, "Flow and heat transfer around a linear array of spheres," *Numer. Heat Transf. Part Appl.*, vol. 26, no. 2, pp. 237–252, 1994.
- [43] T. H. Chilton and A. P. Colburn, "Mass transfer (absorption) coefficients prediction from data on heat transfer and fluid friction," *Ind. Eng. Chem.*, vol. 26, no. 11, pp. 1183–1187, 1934.
- [44] T. H. Chilton and A. P. Colburn, "Distillation and absorption in packed columns A convenient design and correlation method," *Ind. Eng. Chem.*, vol. 27, no. 3, pp. 255–260, 1935.
- [45] E. M. Sparrow and A. L. Loeffler, "Longitudinal laminar flow between cylinders arranged in regular array," *AIChE J.*, vol. 5, no. 3, pp. 325–330, Sep. 1959.
- [46] K. Rehme, "Pressure drop performance of rod bundles in hexagonal arrangements," *Int. J. Heat Mass Transf.*, vol. 15, no. 12, pp. 2499–2517, 1972.
- [47] K. Rehme, "Simple method of predicting friction factors of turbulent flow in non-circular channels," *Int. J. Heat Mass Transf.*, vol. 16, no. 5, pp. 933–950, 1973.
- [48] K. Rehme and G. Trippe, "Pressure drop and velocity distribution in rod bundles with spacer grids," *Nucl. Eng. Des.*, vol. 62, no. 1–3, pp. 349–359, 1980.